Quadrature Control-Bounded ADCs

Hampus Malmberg[1], Fredrik Feyling[2], and Jose M de la Rosa[3]

Dept. of Information Technology & Electrical Engineering, ETH Zürich, Zürich, Switzerland[1]
Dept. of Electronic Systems, Norwegian University of Science and Technology, Trondheim, Norway[2]
Institute of Microelectronics of Seville, IMSE-CNM (CSIC/University of Seville), Seville, Spain[3]

Abstract—In this paper, the design flexibility of the control-bounded analog-to-digital converter principle is demonstrated by considering band-pass analog-to-digital conversion. We show how a low-pass control-bounded analog-to-digital converter can be translated into a band-pass version where the guaranteed stability, converter bandwidth, and signal-to-noise ratio are preserved while the center frequency for conversion can be positioned freely. The proposed converter is validated with behavioral simulations on several filter orders, center frequencies, and oversampling ratios. Finally, robustness against component variations is demonstrated by Monte Carlo simulations.

Index Terms—Analog-to-digital converters, control-bounded, quadrature and band-pass sigma-delta modulation.

I. INTRODUCTION

Band-pass sigma-delta modulators (BP-$\Sigma\Delta$Ms) allow digitizing non-base-band signals; essentially expediting the role and position of analog-to-digital (A/D) conversion in the receiving structure of wireless receivers. A mainly digital wireless receive path is beneficial as digital signal processing offers better technology scaling and programmability towards a software-define-radio (SDR) platform [1]–[3]. Digitizing radio frequency (RF) signals typically utilize sampling frequencies in the GHz range. Hence, state-of-the-art BP-$\Sigma\Delta$Ms are primarily implemented using continuous-time (CT) circuits as they offer inherent anti-aliasing filtering and are potentially faster and more power efficient than their discrete-time (DT) counterparts. However, in the majority of cases, RF BP-$\Sigma\Delta$Ms have a fixed ratio between the center or *notch* frequency, f_n, and the sampling frequency f_s (typically $f_n = f_s/4$). A fixed f_s/f_n ratio results in two main limitations: firstly, for wireless standards operating around 2.5-5GHz, prohibitive values of f_s, in the order of tens of GHz, are typically required. Secondly, a widely programmable phase-locked loop (PLL) is required for tuning f_n while keeping the f_s/f_n ratio fixed. These limitations have prompted the interest in reconfigurable BP-$\Sigma\Delta$Ms with tunable notch frequency [4]. However, reported solutions are limited in practice by the increased (analog) circuit complexity and risk of the potential instability of the loop filter – compromised by the tuning range of f_n [4]. This paper presents an alternative approach to the problem of digitizing RF signals using the so-called control-bounded analog-to-digital converter (CBADC) concept [5], [6]. A quadrature control-bounded analog-to-digital converter (Q-CBADC) is proposed, that offers a highly modular architecture with a tunable f_n and a stability guarantee. In par-

ticular, the Q-CBADC follows from extending two low-pass CBADCs into a single oscillating structure. Conveniently, the Q-CBADC's signal-to-noise ratio (SNR) and bandwidth (BW) specification follows from its two low-pass CBADCs building blocks. Like quadrature sigma-delta modulators (Q-$\Sigma\Delta$Ms) [7], the Q-CBADCs is a quadrature analog-to-digital converter (ADC) resulting in the same number of integrating stages per signal as its low-pass building block.

II. THE LEAPFROG ANALOG FRONTEND

The CBADC concept builds on the idea that an analog system (AS) stabilized by a digital control (DC) amounts to an implicit A/D conversion. As an example of such an AS, consider the system within one of the dashed boxes in Fig. 1. This example shows a low-pass leapfrog (LF) AS [5], parameterized by a forward and feedback gain β and α. To turn the AS into an ADC, it's stabilized by a DC through the control signals $s_1(t), \ldots, s_N(t)$. A CBADC's overall conversion performance follows from the open-loop gain of the AS in combination with a bounded state swing on the state variables $x_\ell(t)$ enforced by the DC—particularly, a large AS gain in combination with a, DC enforced, small state swing result in good conversion performance.

In a subsequent step, the CBADC's final output follows from the control signals as

$$\hat{u}[k] \triangleq \sum_{\ell=1}^{N} (h_\ell * s_\ell)[k]. \tag{1}$$

where the finite impulse response (FIR) filter coefficients $h_1[.], \ldots, h_\ell[.]$, in (1), depend on the parametrization of the analog frontend (AF), i.e., the combined AS and DC. Furthermore, the discrete time control signals in (1) are related to their continuous time counterparts as

$$s_\ell(t) = \sum_k s_\ell[k]\theta_\ell(t - kT) \tag{2}$$

where the DC updates the control signals with a clock frequency of $f_s \triangleq 1/T$ and $\theta(t)$ is the corresponding digital-to-analog converter (DAC) waveform. The FIR filters $h_1[.], \ldots, h_N[.]$ in (1) can be calculated analytically as in [6] or via calibration as in [8]. Beware that component variation in the AS or DC will introduce a significant estimation error if not accounted for in $h_1[.], \ldots, h_N[.]$, cf. [9] and [8].
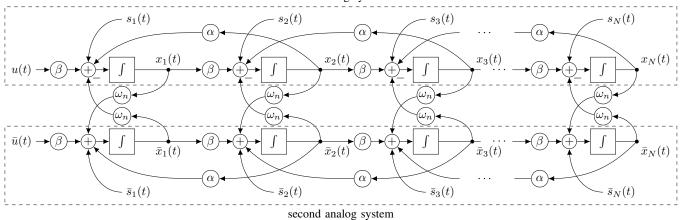
Fig. 1. The quadrature Leapfrog analog system which is is the combination of two Leapfrog structures, as in Section II, connected by the ω_n paths. The system is stabilized via the control signals $s_1(t), \ldots, s_N(t), \bar{s}_1(t), \ldots, \bar{s}_N(t)$ resulting from N quadrature local digital controls as shown in Fig. 2.

The AS is conveniently described using state-space equations; an Nth order LF AS, follows from the differential equations

$$\dot{\boldsymbol{x}}(t) = \boldsymbol{A}_{\text{LF}}\boldsymbol{x}(t) + \boldsymbol{B}_{\text{LF}}u(t) + \boldsymbol{s}(t) \qquad (3)$$

where

$$\boldsymbol{x}(t) \triangleq \big(x_1(t), \ldots, x_N(t)\big)^{\mathsf{T}}, \qquad (4)$$

$$\boldsymbol{s}(t) \triangleq \big(s_1(t), \ldots, s_N(t)\big)^{\mathsf{T}}, \qquad (5)$$

$$\boldsymbol{A}_{\text{LF}} \triangleq \begin{pmatrix} 0 & \alpha & & \\ \beta & 0 & \ddots & \\ & \ddots & \ddots & \alpha \\ & & \beta & 0 \end{pmatrix} \in \mathbb{R}^{N \times N}, \qquad (6)$$

and $\boldsymbol{B}_{\text{LF}} \triangleq (\beta, 0, \ldots, 0)^{\mathsf{T}} \in \mathbb{R}^{N}$.

The LF's homogeneous and modular structure enables design equations where for a given N, $\omega_{\mathcal{B}}$, and oversampling ratio (OSR),

$$\text{SNR} \propto (\text{OSR})^{2N} \qquad (7)$$

and stability follow from the relations

$$|\beta| = \frac{\omega_{\mathcal{B}} \cdot \text{OSR}}{2\pi} \qquad (8)$$

$$\kappa = -\beta = \frac{\omega_{\mathcal{B}}^2}{4\alpha} \qquad (9)$$

where $\omega_{\mathcal{B}}$ [rad/s] is the targeted angular signal bandwidth. [9] showed that the nominal performance of a low-pass LF CBADC is similar to that of a heuristically optimized continuous-time sigma-delta modulator (CT-$\Sigma\Delta$M) with the same loop filter order N, fixed OSR, and the same number of quantization levels.

III. QUADRATURE ANALOG FRONTENDS

Two low-pass CBADCs, as in Section II, can be turned into a quadrature CBADC by two modifications: firstly, interconnecting the two ASs such that they oscillate at the desired notch

frequency f_n, further described in Section III-A. Secondly, the resulting AS can be stabilized by a local quadrature DC, covered in Section III-B. This general principle applies to any low-pass CBADC AF. In the interest of space, only the transformation of the low-pass LF from Section II will be covered in this paper.

A. Quadrature Analog System

For a quadrature AS to oscillate at a desired angular frequency $\omega_n = 2\pi f_n$, two identical Nth order ASs are stacked in parallel and interconnected as

$$\begin{pmatrix} \dot{\boldsymbol{x}}(t) \\ \dot{\bar{\boldsymbol{x}}}(t) \end{pmatrix} = \boldsymbol{A} \begin{pmatrix} \boldsymbol{x}(t) \\ \bar{\boldsymbol{x}}(t) \end{pmatrix} + \boldsymbol{B} \begin{pmatrix} u(t) \\ \bar{u}(t) \end{pmatrix} + \begin{pmatrix} \boldsymbol{s}(t) \\ \bar{\boldsymbol{s}}(t) \end{pmatrix} \qquad (10)$$

$$\boldsymbol{A} \triangleq \begin{pmatrix} \boldsymbol{A}_{\text{LP}} & -\omega_n \boldsymbol{I}_N \\ \omega_n \boldsymbol{I}_N & \boldsymbol{A}_{\text{LP}} \end{pmatrix} \in \mathbb{R}^{2N \times 2N} \qquad (11)$$

$$\boldsymbol{B} \triangleq \begin{pmatrix} \boldsymbol{B}_{\text{LP}} & \boldsymbol{0}_N \\ \boldsymbol{0}_N & \boldsymbol{B}_{\text{LP}} \end{pmatrix} \in \mathbb{R}^{2N \times 2} \qquad (12)$$

where $\boldsymbol{A}_{\text{LP}}$ and $\boldsymbol{B}_{\text{LP}}$ refers to the system description of a low-pass AS, e.g., the $\boldsymbol{A}_{\text{LF}}$ and $\boldsymbol{B}_{\text{LF}}$ from Section II, and $\boldsymbol{x}(t)$, $\bar{\boldsymbol{x}}(t)$, and $\boldsymbol{s}(t)$, $\bar{\boldsymbol{s}}(t)$ are the in-phase and quadrature part of the state vector and control signal vector, respectively. Fig. 1, shows the low-pass LF, from Section II, transformed into its quadrature version.

B. Local Quadrature Digital Control

The quadrature AS, from Section III-A, can be stabilized by N local quadrature DCs as shown in Fig. 2. Here each quadrature state pair $\boldsymbol{x}_\ell(t) \triangleq \big(x_\ell(t), \bar{x}_\ell(t)\big)^{\mathsf{T}}$ are turned into a control observation

$$\tilde{\boldsymbol{s}}_\ell(t) \triangleq \begin{pmatrix} \tilde{s}_\ell(t) \\ \tilde{\bar{s}}_\ell(t) \end{pmatrix} = \begin{pmatrix} \tilde{\kappa}_\phi & -\tilde{\bar{\kappa}}_\phi \\ \tilde{\bar{\kappa}}_\phi & \tilde{\kappa}_\phi \end{pmatrix} \boldsymbol{x}_\ell(t) \qquad (13)$$

which is then sampled and quantized into the quadrature discrete-time control signal pair $\boldsymbol{s}_\ell[k] \triangleq \big(s_\ell[k], \bar{s}_\ell[k]\big)^{\mathsf{T}}$. For a
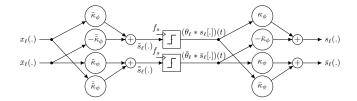
Fig. 2. The ℓth local quadrature DC, connecting $\boldsymbol{x}_\ell(t) = (x_\ell(t), (\bar{x}_\ell(t))$ with $\boldsymbol{s}_\ell = (s_\ell(.), \bar{s}_\ell(.))$ in Fig. 1. The output of the two comparators are considered continuous-time quantities $((\theta_\ell * s_\ell[.])(t), (\bar{\theta}_\ell * \bar{s}_\ell[.])(t))$, where $(\theta_\ell(.), \bar{\theta}_\ell(.))$ are the comparators' impulse responses and $(s[.], \bar{s}[.])$ are the discrete-time control decisions used in (1).

Fig. 3. The coefficients in (18)-(21) as a function of $\omega_n T$ where $2\beta T = 1$, $\phi_\kappa = 0$, and $\tau_{DC} = 0$.

non-return to zero DAC the ℓth quadrature control contribution pair follows as

$$\boldsymbol{s}_\ell(t) \triangleq \begin{pmatrix} s_\ell(t) \\ \bar{s}_\ell(t) \end{pmatrix} = \begin{pmatrix} \kappa_\phi & -\bar{\kappa}_\phi \\ \bar{\kappa}_\phi & \kappa_\phi \end{pmatrix} \boldsymbol{s}_\ell[k] \qquad (14)$$

where $t \in ((k-1)T + \tau_{\text{DC}}, kT + \tau_{\text{DC}}]$ and $\tau_{\text{DC}} > 0$ is the time delay associated with the quantizer.

To determine the required values of κ_ϕ, $\bar{\kappa}_\phi$, $\tilde{\kappa}_\phi$, and $\tilde{\bar{\kappa}}_\phi$ that stabilize the quadrature AS, the derivation of the local low-pass DC, and its stability guarantee, in [5] is extended into the quadrature case. Specifically, $(\kappa_\phi, \bar{\kappa}_\phi, \tilde{\kappa}_\phi, \tilde{\bar{\kappa}}_\phi, T)$ are chosen such that, at the end of a control-period T, each quadrature state pair $\|\boldsymbol{x}_\ell(T)\|_2$ is bounded by a positive constant ϵ for any quadrature input pair $\|\boldsymbol{x}_{\ell-1}(t)\|_2 < \epsilon$, and initial state $\|\boldsymbol{x}_\ell(0)\|_2 < \epsilon$, where $t \in [0, T)$. It follows that if such a parametrization exists, the system as a whole will be inherently stable by a recursive argument given the first quadrature input pair $\|\boldsymbol{x}_0(t)\|_2 \triangleq \| (u(t), \bar{u}(t)) \|_2 < \epsilon$.

These general conditions can be reduced to design equations for the involved parameter values. The steps involved include analytical solutions to differential equations systems and general matrix properties. Given the space limitation, only the resulting expressions will be presented. Simulation results will be shown in Section IV to illustrate and validate the relevance of these mathematical expressions.

1) Matched Signal Strengths: Matching the largest control and input signal contribution reduces to the condition

$$\sqrt{\kappa_\phi^2 + \bar{\kappa}_\phi^2} \stackrel{!}{=} \frac{\beta T \omega_n}{2 \sin \left(\frac{\omega_n T}{2} \right)}. \qquad (15)$$

2) Self Stability: Anticipating and aligning the rotating state trajectories at the end of a control period results in the two conditions

$$\sqrt{\tilde{\kappa}_\phi^2 + \tilde{\bar{\kappa}}_\phi^2} \stackrel{!}{=} \frac{\omega_n}{2\sqrt{\kappa_\phi^2 + \bar{\kappa}_\phi^2} \sin \left(\frac{\omega_n T}{2} \right)} \qquad (16)$$

$$\arctan \left(\frac{\tilde{\bar{\kappa}}_\phi}{\tilde{\kappa}_\phi} \right) \stackrel{!}{=} \omega_n \left(\frac{T}{2} + \tau_{\text{DC}} \right) - \phi_\kappa + \pi, \qquad (17)$$
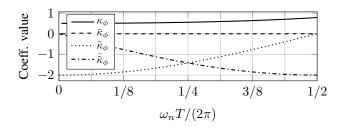
where $\phi_\kappa = \arctan (\bar{\kappa}_\phi / \kappa_\phi)$. By combining (15), (16), and (17) follows

$$\kappa_\phi = \frac{\beta T \omega_n}{2 \sin \left(\frac{\omega_n T}{2} \right)} \cos (\phi_\kappa) \qquad (18)$$

$$\bar{\kappa}_\phi = \frac{\beta T \omega_n}{2 \sin \left(\frac{\omega_n T}{2} \right)} \sin (\phi_\kappa) \qquad (19)$$

$$\tilde{\kappa}_\phi = -\frac{1}{\beta T} \cos \left(\omega_n \left(\frac{T}{2} + \tau_{\text{DC}} \right) - \phi_\kappa \right) \qquad (20)$$

$$\tilde{\bar{\kappa}}_\phi = -\frac{1}{\beta T} \sin \left(\omega_n \left(\frac{T}{2} + \tau_{\text{DC}} \right) - \phi_\kappa \right) \qquad (21)$$

where $\phi_\kappa \in [0, 2\pi)$ is a free parameter that may be chosen to ensure practical values.

3) Worst-Case Superposition: Similarly to the chain-of-integrators case [5],

$$2\beta T \leq 1 \qquad (22)$$

will ensure that the state vector is bounded for a worst-case input and control signal superposition. Fig. 3 demonstrates how κ_ϕ, $\bar{\kappa}_\phi$, $\tilde{\kappa}_\phi$, and $\tilde{\bar{\kappa}}_\phi$ depends on $\omega_n T$ for $2\beta T = 1$, $\phi_\kappa = 0$, and $\tau_{DC} = 0$.

In summary, the stability of a quadrature CBADC analog frontend, as in (10)-(12), can be ensured for $(\kappa_\phi, \bar{\kappa}_\phi, \tilde{\kappa}_\phi, \tilde{\bar{\kappa}}_\phi, T)$ as in (18)-(22).

C. Circuit Implementation Example

To demonstrate that (10)-(14) can be implemented using conventional circuit techniques, Fig. 4 shows a single-ended op-amp implementation of a single quadrature stage from Fig. 1, with a local quadrature control as in Fig. 2. The resistive and capacitive values follow from the RC time constants as $R_\alpha C = \alpha^{-1}$, $R_\beta C = \beta^{-1}$, $R_\kappa C = \kappa^{-1}$, $R_{\bar{\kappa}} C = \bar{\kappa}^{-1}$, $R_{\omega_n} C = \omega_n^{-1}$, $R_{\tilde{\kappa}_I} R_I^{-1} = R_{\tilde{\kappa}_Q} R_Q^{-1} = \tilde{\kappa}$, and $R_{\tilde{\bar{\kappa}}_I} R_I^{-1} = R_{\tilde{\bar{\kappa}}_Q} R_Q^{-1} = \tilde{\bar{\kappa}}$ for $R_I \triangleq R_{\tilde{\kappa}_I} - R_{\tilde{\bar{\kappa}}_I}$, $R_Q \triangleq R_{\tilde{\kappa}_Q} + R_{\tilde{\bar{\kappa}}_Q}$, and $R_{\tilde{\kappa}_I} \geq R_{\tilde{\bar{\kappa}}_I}$. The presented circuit topology does have significant implementation challenges, in particular, the voltage dividers involving $(R_{\tilde{\kappa}_I}, R_{\tilde{\bar{\kappa}}_I}, R_{\tilde{\kappa}_Q}, R_{\tilde{\bar{\kappa}}_Q})$ could be replaced by multi-input comparators and the negative resistors may be managed in a differential setup. However, the purpose of Fig. 4 is to demonstrate that quadrature CBADC reduces to structures similar to CT-$\Sigma\Delta$M circuit implementations.
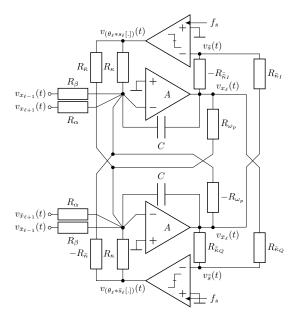
Fig. 4. A single-ended op-amp implementation of a single quadrature stage from Fig. 1 together with a local quadrature control as in Fig. 2.

IV. SIMULATION RESULTS

Behavioral simulations for multiple system specifications were done in Python using the cbadc toolbox [10]. Each simulation used a pair of full-scale input signals, $u(t) = v_{\text{fs}} \cos(2\pi f_s t)$ and $\bar{u}(t) = v_{\text{fs}} \sin(2\pi f_s t)$ for $f_s = f_p - \omega_{\mathcal{B}}/(8\pi)$, $\phi_\kappa = \pi/3$, $\tau_{\text{DC}} = 0$, and $v_{\text{fs}} = 1$V. The final estimate of $u(t)$, in Fig. 1, follows from (1). The corresponding power spectral density (PSD), after computing a 2^{14} point FFT, for OSR/$N = (4/8, 8/6)$ and multiple notch frequencies f_n are shown in Fig. 5. Note that, in contrast to the output of a CT-$\Sigma\Delta$Ms, the CBADC's post-processing filter, (1), implicitly suppresses out-of-band frequencies. The SNRs, measured directly on the resulting PSDs, are approximately 83 and 105 dB, respectively, with variations within ± 1 dB between all notch frequencies. The reported SNRs also agree within ± 1 dB of the corresponding low-pass LF system's performance. The low-pass PSD is shown in blue in Fig. 5.

A significant limiting factor for both BP-$\Sigma\Delta$M and Q-$\Sigma\Delta$M is stability in the presence of component variations while targeting a wide tunable range. The proposed Q-CBADC's sensitivity to component variations was tested by 256 Monte Carlo simulations where each individual $(\alpha, \beta, \omega_n, \kappa_\phi, \bar{\kappa}_\phi, \tilde{\kappa}_\phi, \tilde{\bar{\kappa}}_\phi)$ value were drawn uniformly at random from within $\pm 10\%$ of their nominal values. For these simulations, the system was modeled using Verilog-A and simulated in Cadence Spectre with OSR $= 8, N = 6$ and $f_n = f_s/8$, which corresponded to 105 dB nominal SNR, see Fig. 5 (bottom). The filter coefficients in (1) were calculated from the actual system parametrization to avoid the additional filter mismatch error described in Section II. The equivalent component variation scenario was also simulated for the low-pass LF building block. For the low-pass LF, the component variations resulted
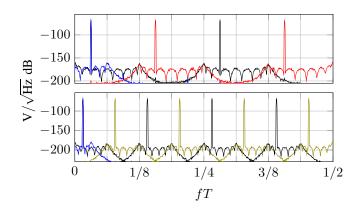

Fig. 5. PSD for different notch frequencies. The black, red, and yellow lines correspond to PSDs of (1) from Q-CBADCs designed for OSR/$N = (4/8, 8/6)$ (top, bottom) and positioned at different notch filter frequencies f_n. Similarly, the blue lines are the PSDs of a corresponding low-pass CBADC building block.
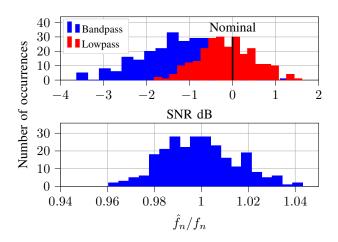

Fig. 6. Histograms showing variation in SNR relative to the nominal performance of 105 dB (top) and estimated $\hat{f}_n$ normalized to nominal $f_n = f_s/8$ (bottom) after 256 Monte Carlo simulations with up to $\pm 10\%$ variations in each $(\alpha, \beta, \omega_n, \kappa_\phi, \bar{\kappa}_\phi, \tilde{\kappa}_\phi, \tilde{\bar{\kappa}}_\phi)$ parameter.

in 3 realizations being unstable and, therefore, significantly reduced SNR. In contrast, none of the Q-CBADC realizations resulted in instability. Histograms of the resulting SNR performance and estimated notch frequencies $\hat{f}_n$, excluding the unstable low-pass realizations, are given in Fig. 6. The results show SNRs and notch frequencies $\hat{f}_n$ in the ranges of $(-4, 2)$ dB, and $\pm 5\%$ from their respective nominal values. We conjecture, that the average reduction of 1 dB SNR, in the Q-CBADC case, originates from the fact that the quadrature stages in Fig. 1 may lose amplification, in the transfer function from $(u(t), \bar{u}(t))$ to $(x_N(t), \bar{x}_N(t))$, by the combined effect of changes in bandwidth and non-aligning resonance frequencies per stage. This differs from the low-pass LF case where the same component variation simulation shows no significant change to average SNR as effectively only the bandwidth per stage varies. How to calibrate the digital estimator (DE), as was effectively assumed in the above simulations, is further described in [8].

V. Conclusions

The Q-CBADC design principle extends any low-pass CBADCs into a quadrature version centered around a desired notch frequency without loss of SNR or stability margin. Nominal performance and tuning range are verified by behavioral simulations of different system orders and OSRs. Robustness is demonstrated by electrical Monte Carlo simulations, with up to 10% component variations, resulting in a performance range of approximately $(-4, 2)$ dB, with respect to the nominal SNR. These results demonstrate that quadrature CBADC is a good alternative for the implementation of RF digitizers with continuous tuning of the notch frequency, opening the doors to more efficient realization of software-defined radios.

References

[1] A. Sayed *et al.*, "A 1.5-to-3.0GHz Tunable RF Sigma-Delta ADC With a Fixed Set of Coefficients and a Programmable Loop Delay," *IEEE Transactions on Circuits and Systems - II: Express Briefs*, vol. 67, pp. 1559–1563, September 2020.

[2] H. Ghaedrahmati, J. Zhou, and R. B. Staszewski, "A 38.6-fJ/Conv.-Step Inverter-Based Continuous-Time Bandpass ΔΣ ADC in 28 nm Using Asynchronous SAR Quantizer," in *IEEE Transactions on Circuits and Systems - II: Express Briefs*, vol. 68, pp. 3113–3117, September 2021.

[3] L. Jie *et al.*, "A 100MHz-BW 68dB-SNDR Tuning-Free Hybrid-Loop DSM with an Interleaved Bandpass Noise-Shaping SAR Quantizer," *IEEE ISSCC Digest of Technical Papers*, February 2021.

[4] G. Molina *et al.*, "LC-Based Bandpass Continuous-Time Sigma-Delta Modulators with Widely Tunable Notch Frequency," *IEEE Trans. on Circuits and Systems – I: Regular Papers*, pp. 1442–1455, May 2014.

[5] H. Malmberg, "Control-Bounded Converters," Ph.D. dissertation no. 27025, ETH Zürich, 2020

[6] H. Malmberg, G. Wilckens, and H.-A. Loeliger, "Control-bounded analog-to-digital conversion," *Circuits, Syst. Signal Process.,* vol. 41, no. 3, pp. 1223-1254, Mar. 2022.

[7] R. Schreier, G. C. Temes, "Bandpass and Quadrature Delta-Sigma Modulation," in *Understanding Delta-Sigma Data Converters*. New York, NY USA: Wiley, 2005, pp. 172-177.

[8] H. Malmberg, T. Mettler, T. Burger, F. Feyling, H.-A. Loeliger, "Calibrating control-bounded ADCs," arXiv:2211.06741v1.

[9] F. Feyling, H. Malmberg, C. Wulff, H.-A. Loeliger, and T. Ytterdal, "High-level comparison of control-bounded A/D converters and continuous-time sigma-delta modulators," in *IEEE Nordic Circuits and Syst. Conf. (NorCAS)*, Oslo, Norway, Oct. 2022, pp. 1-5.

[10] H. Malmberg, Control-Bounded A/D Conversion Toolbox (cbadc), https://github.com/hammal/cbadc.git, v0.2.2, 2022.